Int. J. Heat Mass Transfer. Vol. 35, No. 6, pp. 1455–1467, 1992
Printed in Great Britain

0017–9310/92 $5.00 + 0.00

Velocity and temperature fields in turbulent liquid flow through a vertical concentric annular channel

A. HASAN and R. P. ROY
Department of Mechanical and Aerospace Engineering, Arizona State University, Tempe, AZ 85287, U.S.A.

and

S. P. KALRA
Electric Power Research Institute, Palo Alto, CA 94303, U.S.A.

(*Received* 27 *November* 1990 *and in final form* 28 *May* 1991)

Abstract—Velocity and temperature fields are measured in turbulent upflow of liquid Refrigerant-113 through a vertical concentric annular channel. Data are reported in the Reynolds number range of 18 000–50 300 and inner wall heat flux range of 0–30 000 W m^{-2}. The velocity field measurements are generally successful whereas some difficulty is encountered in the measurement of single-point correlation between turbulent velocity and temperature fluctuations.

INTRODUCTION

SOME EXPERIMENTAL studies of heat and momentum transfer in turbulent liquid flow through heated annuli have been carried out—e.g. Petukhov and Roizen, in gas [1]; Heikal *et al.*, in air [2]; Müller-Steinhagen *et al.*, in liquid heptane [3]; Roy *et al.*, in liquid Refrigerant-113 (R-113) [4]; and Hasan *et al.*, also in liquid R-113 [5]. Experimental studies of turbulent flow through unheated annuli include those of Brighton and Jones, in air [6]; Lawn and Elliott, in air [7]; Rehme, in air [8]; and Wilson, in air [9]. However, there appears to be considerable room for addition of fundamental data on velocity and temperature fields in such flows.

The experimental work reported here is a continuation of our earlier studies [4, 5] of turbulent liquid R-113 upflow through a vertical concentric annular channel with the inner wall heated (constant heat flux) and the outer wall insulated. Measurements of the following quantities were made in the Reynolds number range of 18 000–50 300 and inner wall heat flux range of 0–30 000 W m^{-2} at a channel axial location when the temperature and velocity fields were expected to be fully developed: (1) radial profiles of the time-mean axial and radial velocity components; (2) radial profile of the time-mean temperature; (3) radial profiles of turbulence intensities (velocity components and temperature); (4) radial profile of Reynolds shear stress; and (5) radial profile of the single-point cross-correlation between the radial velocity fluctuation and temperature fluctuation (i.e. turbulent radial heat flux). Simultaneous velocity and temperature fluctuation measurements at heated conditions along with their cross-correlations were performed for the first time. For these experiments, the Grashof number range was 1×10^7–7×10^7. The Gr/Re^2 ratio was always less than 0.1, indicating that the effect of free convection may be neglected.

For brevity, only selected data are presented and discussed. All data have been tabulated comprehensively by Hasan [10].

EXPERIMENTS

The rig and test section

The experimental rig has been described in detail elsewhere [11]. The annular test section was comprised of an outer Pyrex pipe and 304 stainless steel pipe assembly of 38.6 mm i.d. and an inner section of seamless 304 stainless steel tube of 15.9 mm o.d. and 1.25 mm wall. Figure 1 shows, schematically, the part of the test section where the measurements were performed. The initial 0.91 m of the 3.66-m-long test section served as an unheated hydrodynamic entrance length. Heat could be supplied to the remaining 2.75 m length by resistively heating (by d.c., max input power = 60 kW) the inner stainless steel tube. The velocity and temperature measurement plane was approximately 85 hydraulic diameters downstream of the beginning of the heated length. Concentricity of the annulus was maintained by means of four support vane assemblies, each assembly consisting of four 9-mm-long and 1-mm-thick stainless steel vanes arranged in an X configuration, welded to the inner tube at equal spacings. The nearest vane assembly upstream of the measurement plane was about 31 hydraulic diameters away. Concentricity at the measurement section was further ensured by means of a flange with four micrometers installed immediately downstream of the section (not shown in Fig. 1). The

NOMENCLATURE

A_{x-s}	flow area of test section
A, B_0	quantities in equation (1)
C_{uv}	correlation coefficient defined by equation (3)
C_{vt}	correlation coefficient defined by equation (5)
D_h	hydraulic diameter of test section
E	constant temperature anemometer nonlinear bridge output
E^*	constant temperature anemometer nonlinear bridge output after temperature compensation
Gr	Grashof number, $g\beta(\bar{T}_w - \bar{T}_b)D_h^3/\nu^2$
k	thermal conductivity of liquid
m, n	coefficient, exponent in equation (1)
q''_{w_i}	heat flux at annulus inner wall
r	radial coordinate
R^*	nondimensional radial position, $(r-r_i)/(r_o-r_i)$
Re	Reynolds number
$T, \bar{T}$	temperature, time-mean temperature
$\bar{T}_{in}$	mean liquid temperature at test section inlet
$\bar{T}^*$	nondimensional time-mean temperature, $\equiv [\bar{T}-\bar{T}_{in}]k/q''_{w_i}D_h$
t	temperature fluctuation
$\bar{U}, \bar{V}$	time-mean axial velocity, time-mean radial velocity
U_{eff}	effective cooling velocity for anemometer sensor, equation (1)
$\bar{U}^*, \bar{V}^*$	nondimensional time-mean axial velocity, $\equiv \bar{U}/\bar{U}_{max}$, nondimensional time-mean radial velocity, $\equiv \bar{V}/\bar{U}_{max}$
u, v	axial velocity fluctuation, radial velocity fluctuation
$(\overline{u^2})^{0.5}, (\overline{v^2})^{0.5}, (\overline{t^2})^{0.5}$	turbulence intensities
$\overline{uv}$	Reynolds shear stress
$\overline{ut}$	single-point cross-correlation between axial velocity and temperature fluctuations
u_{τ_o}	friction velocity at the outer wall of annulus
$\overline{vt}$	single-point cross-correlation between radial velocity and temperature fluctuations.

Greek symbols

α	radius ratio, r_i/r_o
β	volumetric coefficient of thermal expansion
ν	kinematic viscosity
ρ	liquid density.

Subscripts

b	bulk liquid
e	local liquid
f	film
i, o	annulus inner wall, outer wall
s	sensor
w	heated wall.

heater tube was filled with aluminum oxide powder insulation. The outer section of the annular channel was insulated with 50-mm-thick jacketed fiberglass wool.

The heat flux imposed at the inner wall of the annulus during any experiment was calculated as the ratio of the product of the measured voltage drop across the heater tube and the current through it (also measured) and the tube surface area. Heat balance calculations based on the liquid mass flow rate through the test section and the increase in the mixed-mean temperature of the liquid always accounted for the heat generated in the tube wall to within $\pm 2\%$.

Instrumentation and calibrations

Figure 1 also shows, schematically, the locations of a miniature three-sensor hot-film anemometer probe (TSI 1295AK-10W) and a chromel–constantan microthermocouple (P. Beckman Co., μTC-PB-03) in the measurement section. Two (of a total of four) copper–constantan surface thermocouples (STC) used to measure the heated tube surface temperature are also shown.

Each of the three anemometer sensors of the probe (see inset, Fig. 1) was 25 μm in diameter and 0.44 mm long.† The spanwise separation between sensors 1 and 2 (the x-sensors) was 0.75 mm. This ensured that sensor 3 was not obstructed by the x-sensors. The measurement volume of this probe, if represented by a right circular cylinder of appropriate dimensions with its axis parallel to the z-coordinate, was approximately 0.5 mm^3. The x-sensors were operated in the constant temperature anemometer (CTA) mode with both sensors maintained at 71°C, their temperature being limited by the consideration that incipience of boiling must be prevented at the sensors. The liquid temperature at the measurement plane was typically between 37 and 44°C so that the 'overheat ratio' of the sensors during velocity measurements was adequate. Sensor 3 was operated in the resistance thermometer (constant current) mode for measurement of liquid temperature.

The voltage output of a CTA bridge is a function of both the velocity and temperature of the ambient fluid at the sensor location. Therefore, in order that the velocity may be correctly measured in a noniso-

† The sensor length and spacing were carefully measured by us with the help of a microscope at a magnification of 50.

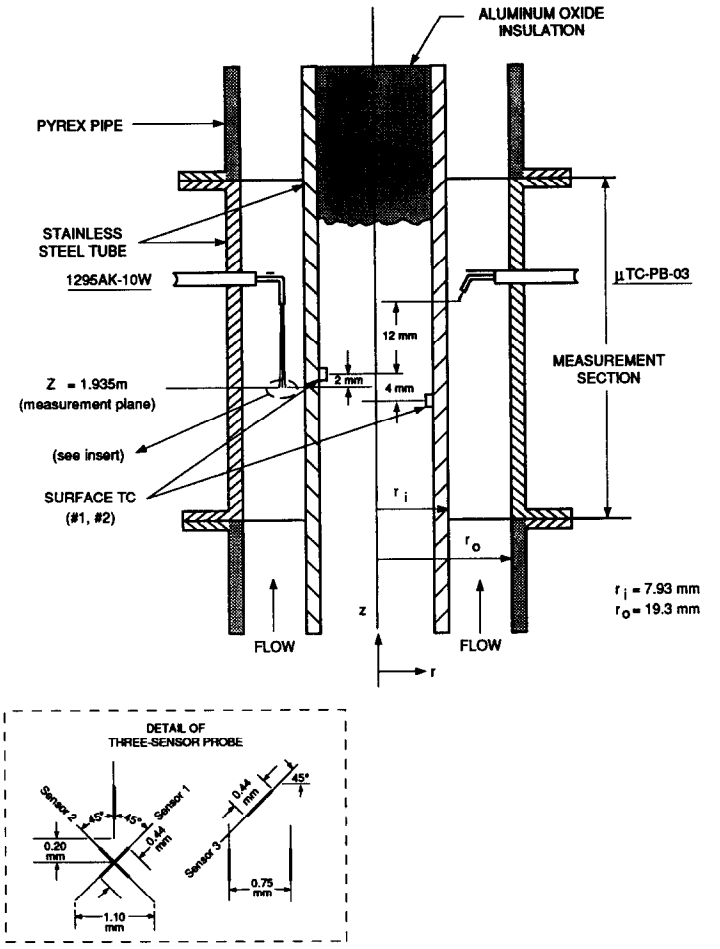

FIG. 1. The annular test section.

thermal flow field the output must be rendered independent of the fluid temperature. To this end, two temperature compensation circuits, similar in principle to one reported by Chevray and Tutu [12], were built to permit on-line compensation of the CTA outputs (one for each of the x-sensors). Considerable care was required to simulate the variation, with ambient liquid temperature, of the parameter A in the CTA nonlinear response equation

$$E^{*2} \equiv \frac{E^2}{T_s - T_c} - A = B_0 U_{\text{eff}}^n \tag{1}$$

as it was found that A is a nonlinear function of T_f, the film temperature ($\equiv (T_s + T_c)/2$). The parameter B_0 was, fortunately, found to be essentially invariant with T_f.

Each temperature-compensated CTA output signal, E^*, was linearized on-line by means of a polynomial linearizer (TSI 1052). Extensive velocity calibrations of the x-sensors were then carried out. The invariance of the velocity calibrations with respect to the ambient liquid temperature was verified over the temperature range of our experiments.

Temperature calibration of sensor 3 was performed *in situ* by increasing the liquid temperature in the test section in stages by means of an upstream preheater and by controlling the heat removed through the rig heat exchanger. The test section itself was unheated. The microthermocouple, which had been calibrated earlier in a constant temperature bath, provided the reference temperature during this calibration. The heater tube surface thermocouples were also calibrated *in situ* in this manner.

There was some concern as to whether the temperature response of a 10 W hot-film sensor (such as sensor 3 of the CTA probe) was fast enough to be able to follow the liquid temperature fluctuations at the high end of the frequency spectrum (e.g. 100–200 Hz). To explore this, a test apparatus was constructed. It consisted of a 13.6 mm by 13.6 mm square channel, 0.45 m in length, through which liquid R-113 at a constant temperature could be pumped at various flow rates. Three sides of the channel were of aluminum and the fourth side of transparent glass. A miniature CTA probe equipped with a single 10 W hot-film sensor (TSI 1262-10W) was inserted through an aluminum side such that the sensor was at the midpoint of the square channel at an axial location

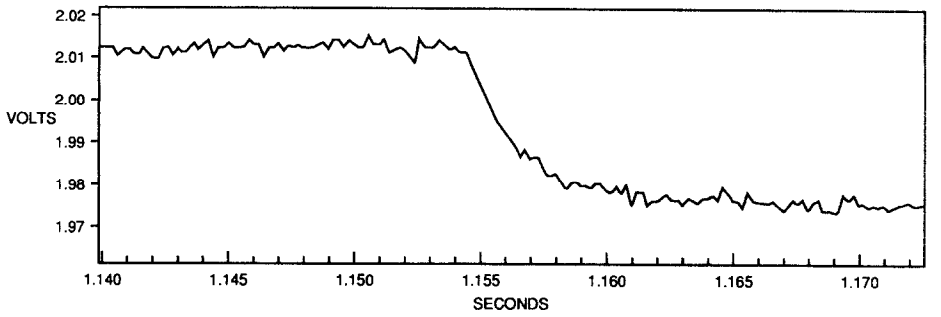

(a) Response of 10W sensor to step removal of heat input (laser).

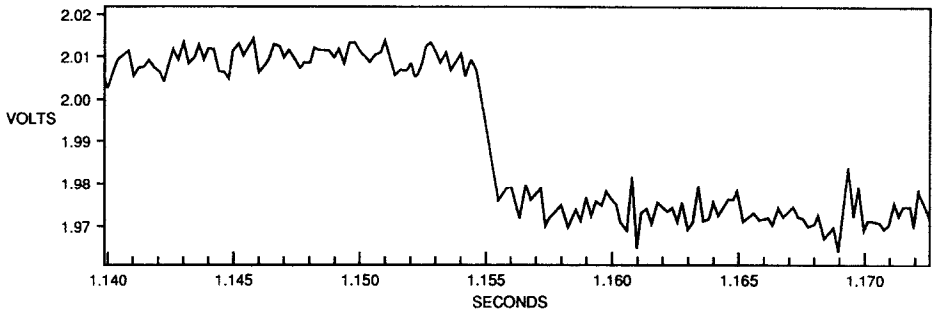

(b) Response of 10W sensor (phase-compensated) to step removal of heat input (laser).

FIG. 2. Transient response of the 10 W hot-film temperature sensor.

approximately 0.39 m downstream of the flow entrance. The sensor was operated in the resistance thermometer (constant current) mode. The liquid flow rate through the channel was measured by a turbine flow meter (Flow Technology). A 15 mW He–Ne laser (Melle-Groit) beam was directed through a Nikon DW-1 shutter (closing time <1 ms) so as to impinge on the sensor through the glass side of the channel. The sensor temperature increased gradually until a steady state was reached. The shutter was then closed suddenly causing complete blockage of the laser beam. The transient response of the sensor to this essentially step removal of heat input was recorded in a data acquisition system and the sensor time constant determined from the response. Figure 2(a) depicts a typical response of the sensor. Figure 3 (the open square symbols and the dashed line) shows the variation of the sensor time constant with the local fluid velocity as well as the corresponding Reynolds number based on the channel mixed-mean velocity. The speed of response of the sensor to a step change in the ambient liquid temperature was thus indirectly estimated.

It was decided that the sensor time constant (e.g. ≈ 7 ms at a local R-113 velocity of 0.7 m s^{-1}) was too large for the sensor to follow, without significant attenuation and phase lag, the higher frequency liquid temperature fluctuations during the turbulent flow experiments. To improve the sensor frequency

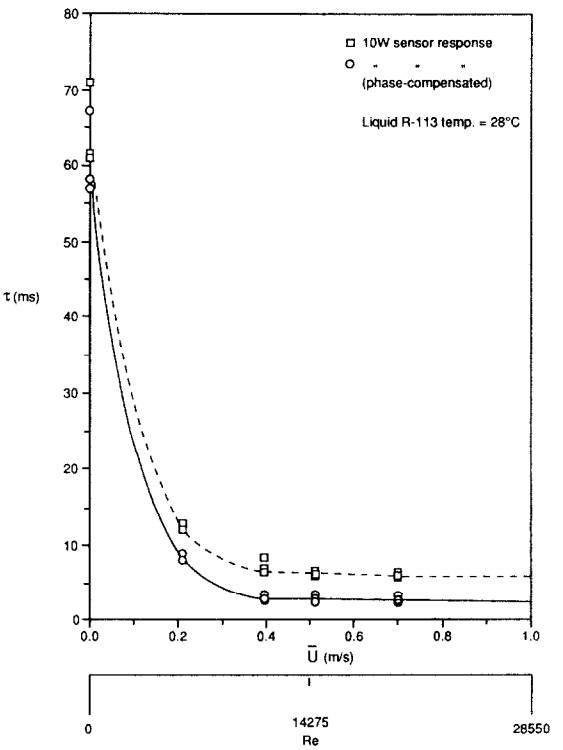

FIG. 3. Time constant of the 10 W hot-film temperature sensor.

Table 1. Range of experiments and measurement uncertainties†

	Range	Uncertainty
Mixed-mean velocity/Reynolds number	0.32–0.80 m s^{-1}/18 000–50 300	±0.006 m s^{-1}
Wall heat flux	0–30 000 W m^{-2}	±80 W m^{-2}
Wall (heated) temperature	40.9–82.6°C	±0.4°C
Mean liquid temperature (local) at measurement plane	37.0–43.0°C	±0.2°C
Liquid pressure at measurement plane	219–302 kPa	±0.7 kPa
Mean liquid temperature at test section inlet	35.4–42.2°C	±0.1°C
Sensor radial traverse	0–10 mm	±30 μm

† The uncertainty estimates are for 95% confidence.

response, an 'active phase-lead compensation circuit' similar in principle to one proposed by Hishida and Nagano [13] was built. The transfer function of this circuit (i.e. gain and phase lead versus frequency) was tailored to the 10 W sensor characteristics. Figure 2(b) shows the improved response of the compensated sensor to a step removal of heat input identical to the Fig. 2(a) case at the same forced convection conditions. Figure 3 (the open circles and the solid line) shows the shorter time constant of the phase-compensated 10 W sensor (e.g. ≈3 ms at a local velocity of 0.7 m s^{-1}). All temperature measurements presented in this paper were performed by means of sensor 3 of the CTA probe compensated by the aforementioned circuit.

A dedicated system (DATA 6000A, Analogic) with a floppy disk drive and plotter peripherals was used to acquire, store, analyze and display the time series data for velocity and temperature.

Tests

Table 1 shows the range of variables over which the measurements were conducted and the associated uncertainties.

For each experiment series (as defined by the Reynolds number, pressure, and temperature in the test section), a set of wall heat fluxes beginning from zero was chosen. A steady state was established in the test section at each heat flux. The heated wall temperature was measured by STC 1 and STC 2. The three-sensor hot-film probe was manually traversed along the radial coordinate and the following quantities were measured at each radial location:

mean liquid axial velocity, $\bar{U}$
mean liquid radial velocity, $\bar{V}$
mean liquid temperature, $\bar{T}$
turbulence intensities, $(\overline{u^2})^{0.5}$, $(\overline{v^2})^{0.5}$, $(\overline{t^2})^{0.5}$
Reynolds shear stress, $\overline{uv}$
single-point cross-correlation between radial velocity and temperature fluctuations, $\overline{vt}$.

Table 2 contains the measured range of values of the turbulence quantities and the uncertainties associated with them. The uncertainties were estimated by the method of Kline and McClintock [14].

The mixed-mean liquid temperature at the measurement plane was calculated as

$$\bar{T}_b = \frac{\int_{A_{x-s}} \bar{U}(r)\bar{T}(r)\,dA}{\int_{A_{x-s}} \bar{U}(r)\,dA}. \quad (2)$$

Table 2. Range of turbulence quantities and associated uncertainties†

	Range	Uncertainty
Axial velocity fluctuation intensity	0.014–0.068 m s^{-1}	±0.001 m s^{-1}
Radial velocity fluctuation intensity	0.010–0.053 m s^{-1}	±0.001 m s^{-1}
Reynolds shear stress	(-850×10^{-6})–(1160×10^{-6}) $m^2 s^{-2}$	$\pm15\times10^{-6}$ $m^2 s^{-2}$ for magnitudes $<100\times10^{-6}$ $m^2 s^{-2}$; to $\pm60\times10^{-6}$ $m^2 s^{-2}$ for magnitudes $>400\times10^{-6}$ $m^2 s^{-2}$
Temperature fluctuation intensity	0.1–1.2°C	±0.005°C
Cross-correlation between radial velocity and temperature fluctuations	1.8×10^{-3}–7.3×10^{-3} m °C s^{-1}	$\pm0.3\times10^{-3}$ m °C s^{-1} for magnitudes $<4.0\times10^{-3}$ m °C s^{-1}; to $\pm0.6\times10^{-3}$ m °C s^{-1} for magnitudes $>4.0\times10^{-3}$ m °C s^{-1}

† The uncertainty estimates are for 95% confidence.

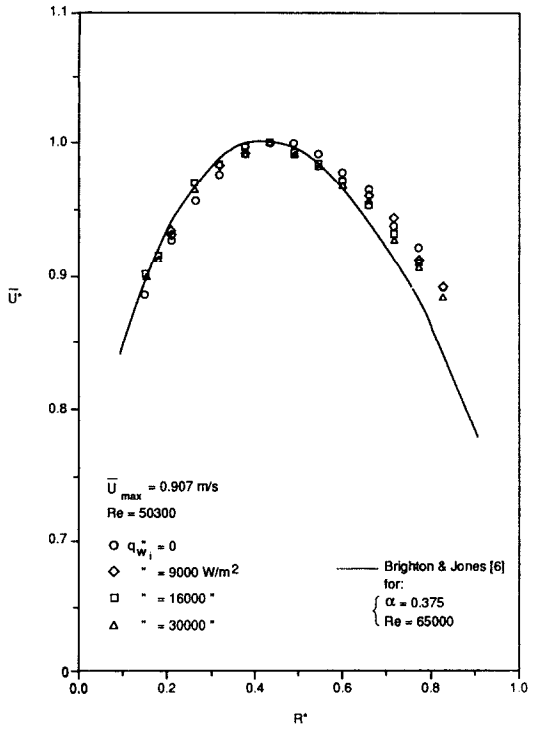

FIG. 4. Mean axial velocity profiles at Reynolds number of 50 300.

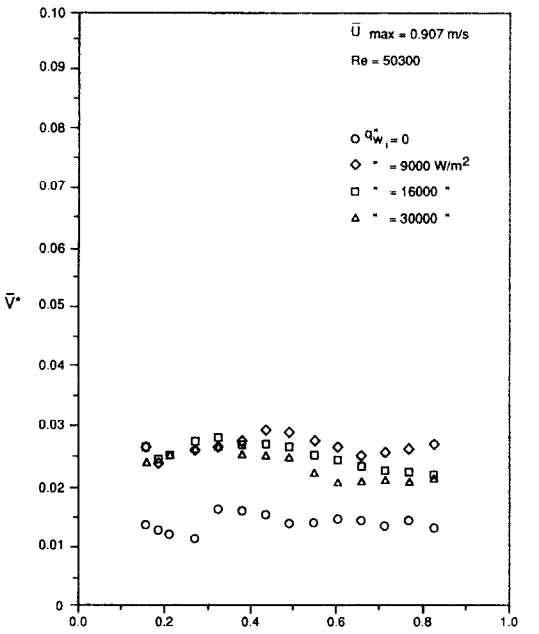

FIG. 5. Mean radial velocity profiles at Reynolds number of 50 300.

This temperature was used in the determination of various liquid properties, such as density, thermal conductivity, viscosity and specific heat.

RESULTS AND DISCUSSION

Figure 4 is a plot of the nondimensional mean liquid axial velocity $\bar{U}^*$ versus the nondimensional radial position R^* for a Reynolds number of 50 300. Data from unheated as well as heated (at heat fluxes of 9000, 16 000 and 30 000 W m^{-2}) experiments are shown. A velocity profile based on the data of Brighton and Jones [6] for a Reynolds number of 65 000 in an annulus of radius ratio, α, of 0.375 is shown for comparison, the radius ratio being 0.411 in our case. The data show expected trends such as a maximum at $R^* \approx 0.4$.† The one deviation from the Brighton and Jones profile is the less steep decrease in our profile as the outer wall of the annulus is approached.

Figure 5 is a plot of the nondimensional mean liquid radial velocity $\bar{V}^*$ versus R^* for the same experimental conditions as in Fig. 4. In a fully developed flow of a constant-property fluid, the mean radial velocity should be zero. We measure nonzero values of this velocity especially in the heated cases although they are quite small compared to the axial velocity component. In the core region of the flow, the mean radial velocity is about 2–3% of the mean axial velocity in the heated cases. The wall heat flux and the accompanying temperature and fluid property (e.g. density and viscosity) variations clearly have a significant influence in this regard. Note that the zero heat flux (isothermal) data exhibit the smallest radial velocities.

Measurements such as those shown in Figs. 4 and 5 were also performed at Reynolds numbers of 18 000, 24 000, 33 400 and 40 200. The data exhibit similar characteristics and are not presented here for brevity.

Figure 6 shows radial profiles of the nondimensional mean liquid temperature $\bar{T}^*$ for Reynolds numbers of 33 400 and 50 300 at several wall heat fluxes. The corresponding heated wall temperatures are also shown. The data for the different wall heat fluxes collapse well at each Reynolds number. Some effort towards finding a suitable nondimensionalization that would cause all of the data to collapse was made with limited success [10].

Mean liquid temperature profile measurements were also carried out at Reynolds numbers of 18 000, 24 400 and 40 200. The data trends were essentially the same.

Figures 7(a) and (b) show, respectively, radial profiles of the turbulence intensities $(\overline{u^2})^{0.5}$ and $(\overline{v^2})^{0.5}$ measured at unheated conditions for Reynolds numbers of 18 000, 24 400, 33 400, 40 200 and 50 300. The dimensional values are shown to allow a feel for the magnitudes of these intensities. When the same data are plotted as $(\overline{u^2})^{0.5}/u_{\tau_o}$ and $(\overline{v^2})^{0.5}/u_{\tau_o}$, the data collapse reasonably well in a narrow band. u_{τ_o}, the friction velocity at the outer wall, was estimated by a best-fit curve through the Reynolds shear stress data presented later.

† The maximum axial velocity location was in the R^* range of 0.40–0.43 for the Reynolds numbers studied here.

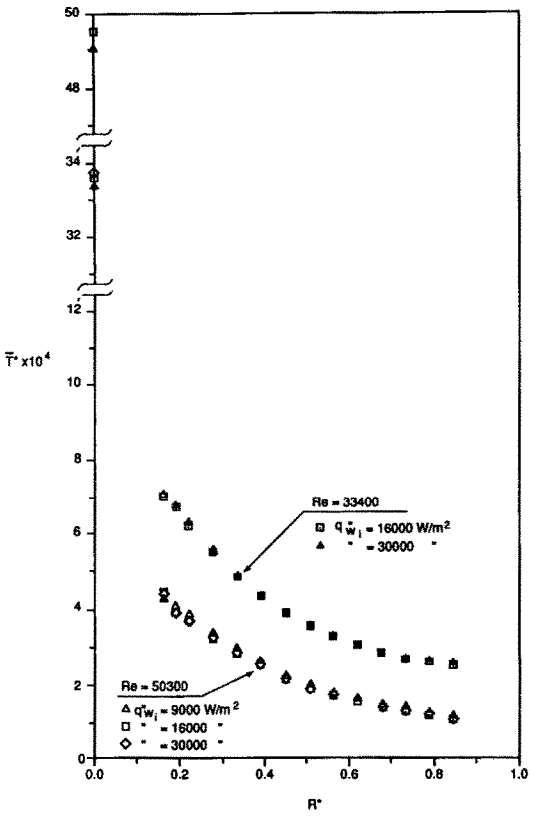

FIG. 6. Mean temperature profiles at Reynolds numbers of 33 400 and 50 300.

Figures 7(a) and (b) exhibit two trends worthy of note: (i) the turbulence intensities increase with the Reynolds number, and (ii) the locations of the minima in their profiles are near the maximum mean axial velocity locations.† Both these trends are in agreement with Brighton and Jones [6] and Roy *et al.* [4]. In general, however, our intensity magnitudes are larger (by 10–40%) than those of Brighton and Jones [6].

Figures 8(a) and (b) show, respectively, the radial profiles of the turbulence intensities $(\overline{u^2})^{0.5}$ and $(\overline{v^2})^{0.5}$ for a Reynolds number of 50 300 at wall heat fluxes of 9000, 16 000 and 30 000 W m^{-2}. The unheated data at the same Reynolds number, shown earlier in Figs. 7(a) and (b), are also shown for comparison. A monotonic increase in the intensities with wall heat flux is observed. The increase is significantly larger toward the heated (inner) wall compared to the outer wall vicinity. Moreover, the locations of the minima in these profiles shift toward the outer wall with the application of wall heat flux. All of these trends were observed at the other Reynolds numbers (namely 18 000, 24 400, 33 400 and 40 200) as well.

Figure 9 shows liquid temperature fluctuation intensity profiles at a Reynolds number of 50 300 and

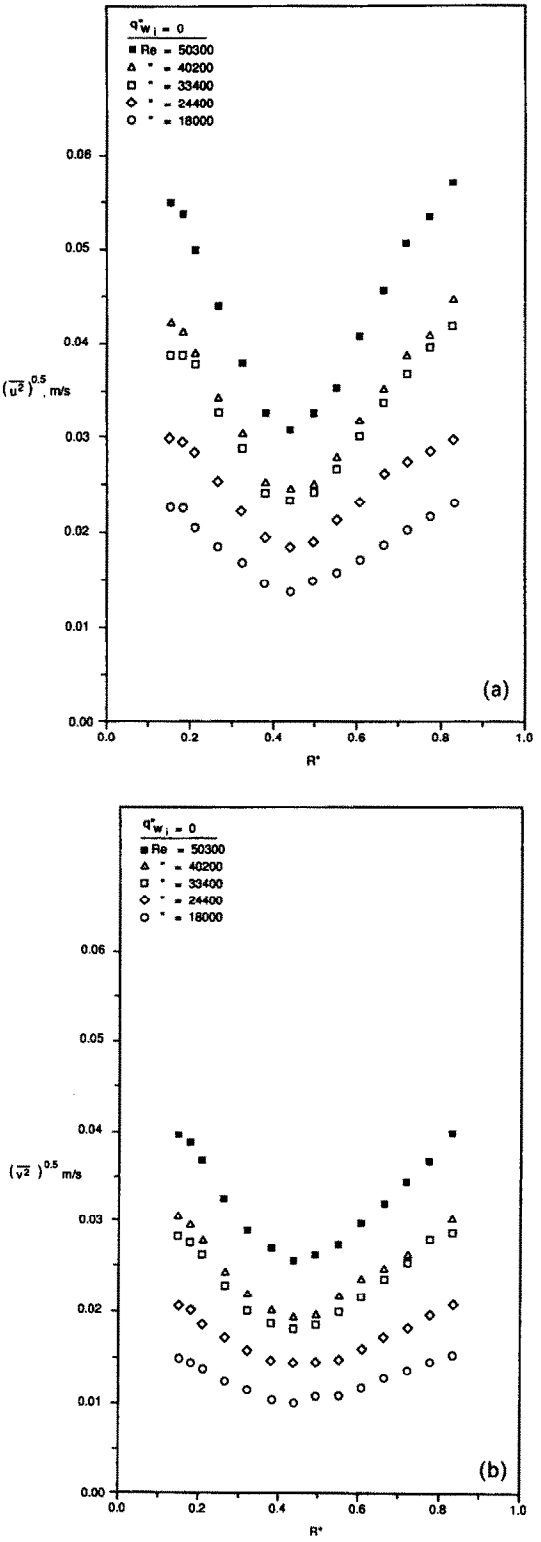

FIG. 7. Velocity fluctuation intensity profiles at the unheated condition.

wall heat fluxes of 9000, 16 000 and 30 000 W m^{-2}. The intensity has been nondimensionalized by $(\bar{T}_w - \bar{T})$, the differential between the mean heated wall temperature and the local mean liquid tempera-

† These locations, when determined from profiles such as in Figs. 4 and 7, have rather large uncertainties associated with them, however.

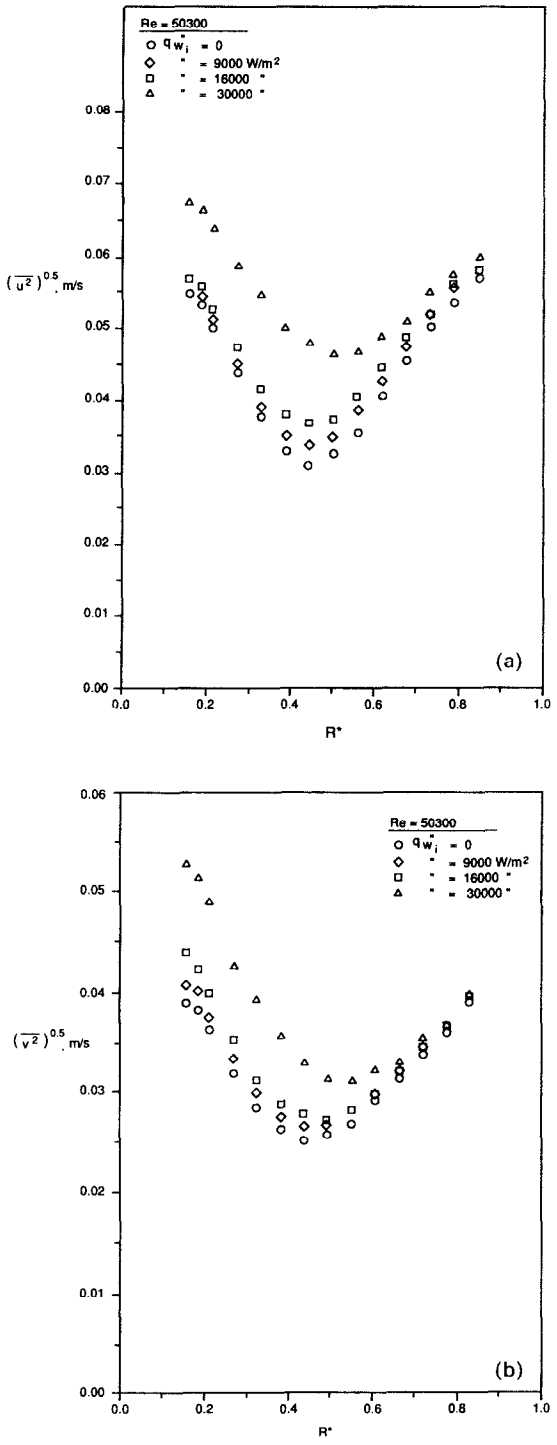

FIG. 8. Velocity fluctuation intensity profiles at a Reynolds number of 50 300 and various wall heat fluxes.

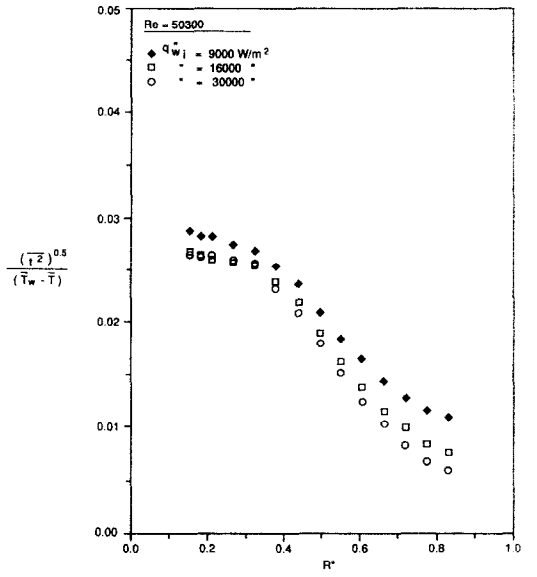

FIG. 9. Temperature fluctuation intensity profiles at a Reynolds number of 50 300.

ture. This temperature differential has been referred to by Burchill [15] as the driving potential for the local liquid temperature fluctuations. Some collapse of the data can be observed in the figure. Some of the characteristics of liquid temperature intensity profiles at various Reynolds numbers and wall heat fluxes have been discussed in our earlier papers [4, 5].

Figure 10(a) contains radial profiles of the Reynolds shear stress $\overline{uv}$, in dimensional form, measured at unheated conditions for Reynolds numbers of 18 000, 24 400, 33 400, 40 200 and 50 300. The Reynolds shear stress is, as expected, negative in the region where the radial gradient of the mean axial velocity is positive, and positive where the gradient is negative. Furthermore, it equals zero at $R^* \approx 0.40$–0.42, which is very close to the location of the maximum axial velocity. The data also exhibit the trend of increasing Reynolds shear stress as the Reynolds number increases.

The nondimensionalized (by $u_{\tau o}^2$, the square of the friction velocity at the outer wall for the corresponding Reynolds number) plots of the same Reynolds shear stress data are shown in Fig. 10(b). While there is some scatter near the inner wall, the collapse is reasonably good. A shear stress profile obtained from the data of Brighton and Jones [6] for an annulus of radius ratio 0.375 and Reynolds number of 65 000 is also shown for comparison.

An indication that a good estimate of friction velocity at the outer wall, $u_{\tau o}$, was obtained is as follows: the ratio $\bar{U}_b/u_{\tau o}$, where $\bar{U}_b$ was calculated from the measured axial velocity profile, was ≈ 21–22 in our case. This is comparable to the value of about 25 obtained by Wilson [9].

The correlation coefficient C_{uv}, defined as

$$\frac{\overline{uv}}{(\overline{u^2})^{0.5}(\overline{v^2})^{0.5}} \tag{3}$$

was calculated for all data shown in Fig. 10(a). This coefficient, by virtue of its definition, lies between -1 and $+1$ and its magnitude is indicative of the degree of correlation (interdependence) between u and v. The

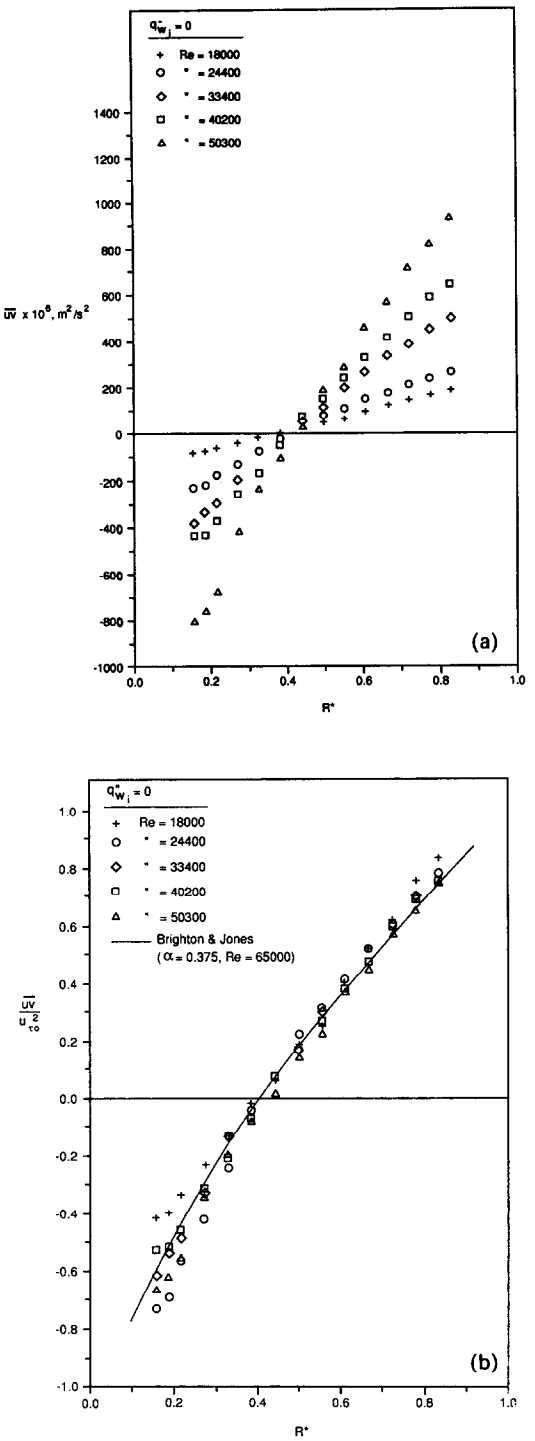

FIG. 10. (a) Reynolds shear stress profiles at the unheated condition for various Reynolds numbers. (b) Non-dimensional Reynolds shear stress profiles at the unheated condition for various Reynolds numbers.

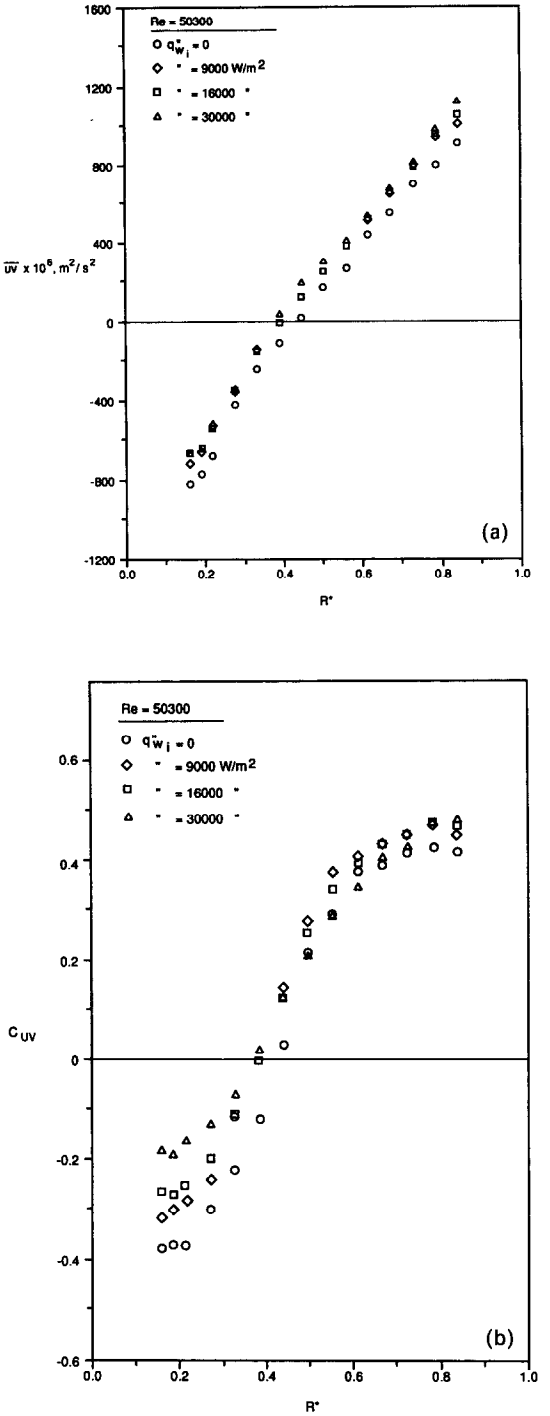

FIG. 11. (a) Reynolds shear stress profiles at a Reynolds number of 50 300 and various wall heat fluxes. (b) Axial velocity–radial velocity correlation coefficient profiles at a Reynolds number of 50 300 and various wall heat fluxes.

magnitude $|C_{uv}|$ was found to be in the range 0–0.5 for all of our data. This compares well to the pipe flow results of Hishida *et al.* [16] and Bremhorst and Bullock [17], the flat plate results of Subramanian and Antonia [18], and the annulus results of Rehme [8].

Figure 11(a) shows radial profiles of Reynolds shear stress at a Reynolds number of 50 300 and wall heat fluxes of zero, 9000, 16 000 and 30 000 W m^{-2}. One discernible effect of the imposition of wall heat flux is a shift of the zero shear stress location closer to the heated wall. There is a concomitant decrease in

the magnitude of the shear stress in the region between the zero crossing point and the inner wall and an increase in the region between the zero crossing point and the outer wall. The latter trends match the changes in the mean axial velocity profile caused by the imposition of heat flux (see Fig. 4—the profile becomes slightly flatter near the inner wall and slightly steeper near the outer wall upon introduction of heat flux). However, whether there is any significant shift in the radial location of the maximum axial velocity point due to the imposition of wall heat flux is unclear from the data.

Reynolds shear stress measurements at various wall heat fluxes were also performed for Reynolds numbers of 18 000, 24 400, 33 400 and 40 200. The data trends are generally the same [10].

Figure 11(b) contains plots of the correlation coefficient C_{ut} at a Reynolds number of 50 300 and wall heat fluxes of zero, 9000, 16 000 and 30 000 W m^{-2}. The wall heat flux is seen to have a distinct influence on the correlation coefficient in the heated wall proximity in that its magnitude decreases as the heat flux increases. On the other hand, the effect is significantly less towards the outer (unheated) wall. The correlation coefficient exhibits the same characteristics at the other Reynolds numbers investigated, namely 18 000, 24 400, 33 400 and 40 200.

Figure 12 shows radial profiles of the single-point cross-correlation between the radial velocity and temperature fluctuations, $\overline{vt}$, nondimensionalized by $(q''_{w_1}/\rho c_p)$, for the following conditions:

Reynolds number:

$$\left.\begin{matrix}24\,400\\33\,400\\40\,200\\50\,300\end{matrix}\right\}\ \text{at wall heat flux of } 16\,000\ \text{W m}^{-2}$$

and

$$\left.\begin{matrix}18\,000\end{matrix}\right\}\ \text{at wall heat flux of } 9000\ \text{W m}^{-2}.$$

Also shown is $\overline{vt}/(q''_{w_1}/\rho c_p)$ profile calculated from the local heat balance equation [10]

$$\frac{\overline{vt}(r)}{q''_{w_1}/\rho c_p} = \frac{r_1}{r}\cdot\frac{\int_r^{r_0}\bar{U}r\,\mathrm{d}r}{\int_{r_1}^{r_0}\bar{U}r\,\mathrm{d}r} + \frac{k}{q''_{w_1}}\cdot\frac{\partial\bar{T}}{\partial r} + \frac{\bar{V}}{q''_{w_1}r}\cdot\int_r^{r_0}\frac{\partial\bar{T}}{\partial r}r\,\mathrm{d}r + \frac{\rho c_p}{q''_{w_1}r}\int_r^{r_0}\frac{\partial}{\partial z}(\overline{ut})r\,\mathrm{d}r. \quad (4)$$

An assumption of azimuthal symmetry is inherent in equation (4). Also, the last term on the right hand side of equation (4) was assumed to be small and was neglected. The profiles calculated for the cases listed above overlap to yield an essentially single profile.

Figure 13 depicts radial profiles of the nondimensionalized $\overline{vt}$ correlation for the following conditions:

wall heat flux:

$$\left.\begin{matrix}9000\ \text{W m}^{-2}\\16\,000\ \text{W m}^{-2}\\30\,000\ \text{W m}^{-2}\end{matrix}\right\}\ \text{at a Reynolds number of 50 300.}$$

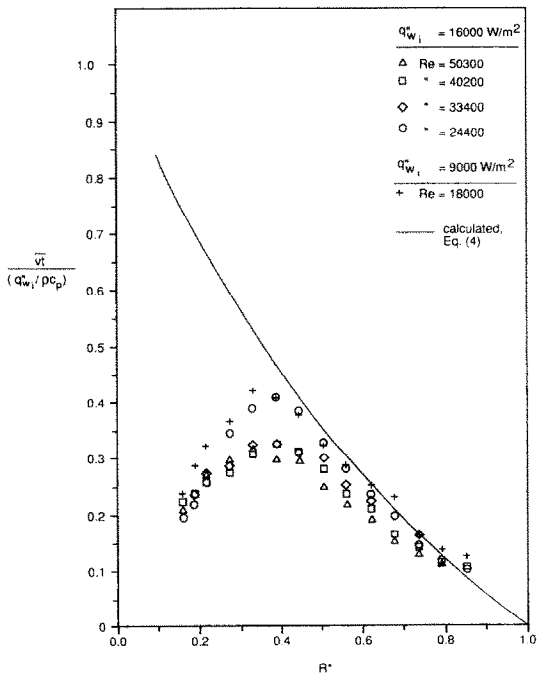

FIG. 12. Nondimensional radial velocity–temperature correlation profiles at various Reynolds numbers and wall heat fluxes.

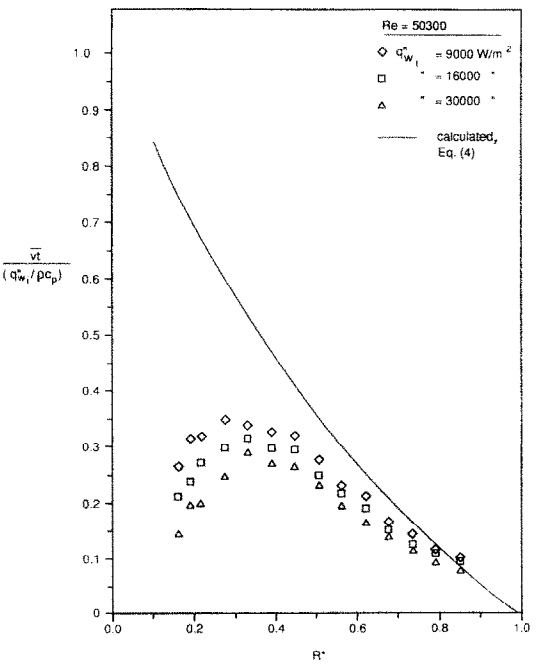

FIG. 13. Nondimensional radial velocity–temperature correlation profiles at Reynolds number of 50 300 and various wall heat fluxes.

The calculated profile of the nondimensionalized $\overline{vt}$ correlation, which represents all three cases, is also shown.

It is clear from Figs. 12 and 13 that we were unable to measure the $\overline{vt}$ correlation correctly in the region $R^* < 0.4$. A discussion regarding this is presented later.

Figure 14(a) contains plots of the correlation coefficient C_{vt}, defined as

$$\frac{\overline{vt}}{(\overline{v^2})^{0.5}(\overline{t^2})^{0.5}} \tag{5}$$

at a wall heat flux of 16000 W m^{-2} and Reynolds numbers of 24400, 33400, 40200 and 50300. A diminution in the magnitude of the correlation as the heated wall is approached is evident although no clear trend with respect to Reynolds number can be identified.

Figure 14(b) shows plots of C_{vt} at a Reynolds number of 50300 and wall heat fluxes of 9000, 16000 and 30000 W m^{-2}. A diminution in the degree of correlation is observed toward the heated wall as the heat flux increases.

Several reasons may be suggested for our difficulty with the measurement of the $\overline{vt}$ correlation. One involves the relatively large measurement volume of the three-sensor probe in comparison to the extent of the annulus gap (Fig. 1).† Now, the size of the energy-carrying eddies in turbulent flow through the annular channel range from the gap dimension ($\approx$11 mm) down to the Kolmogorov length scale which diminishes as the Reynolds number increases. Furthermore, for liquids such as R-113 whose Prandtl number is considerably larger than 1, the temperature fluctuations extend down to scales which are significantly smaller than the smallest velocity length scales. Also, the steepest temperature gradients are associated with the smallest eddies [19]. These considerations suggest that difficulty would be experienced in measuring the velocity–temperature correlations by relatively bulky probes. We also note that the temperature sensor (No. 3) was 0.75 mm downstream of the velocity sensors. The sensors may have been too far apart, especially in the steep temperature gradient regions, to allow correct measurement of velocity–temperature correlations. On the other hand, our velocity correlation data (Figs. 10 and 11) indicate that these particular measurements were successful.

Another reason concerns possible interference of the temperature sensor by the x-sensors (e.g. via wakes and heated plumes from the latter). From a purely dimensional consideration, this ought not have been a problem because the projected length of sensor No. 3 in the r–θ (cross-sectional) plane was smaller than the spanwise spacing between the x-sensors. A simple test partly verified this: sensor 2 was operated as a second temperature sensor while sensor 1 still functioned in the velocity mode (only one heated plume, from sensor 1, emanated now). Sensor 3 measurements of the temperature fluctuations remained essentially identical to those obtained with both x-sensors in the velocity mode.

A question may also be raised as to whether the aforementioned situation influenced the temperature compensation of the two velocity sensor signals,

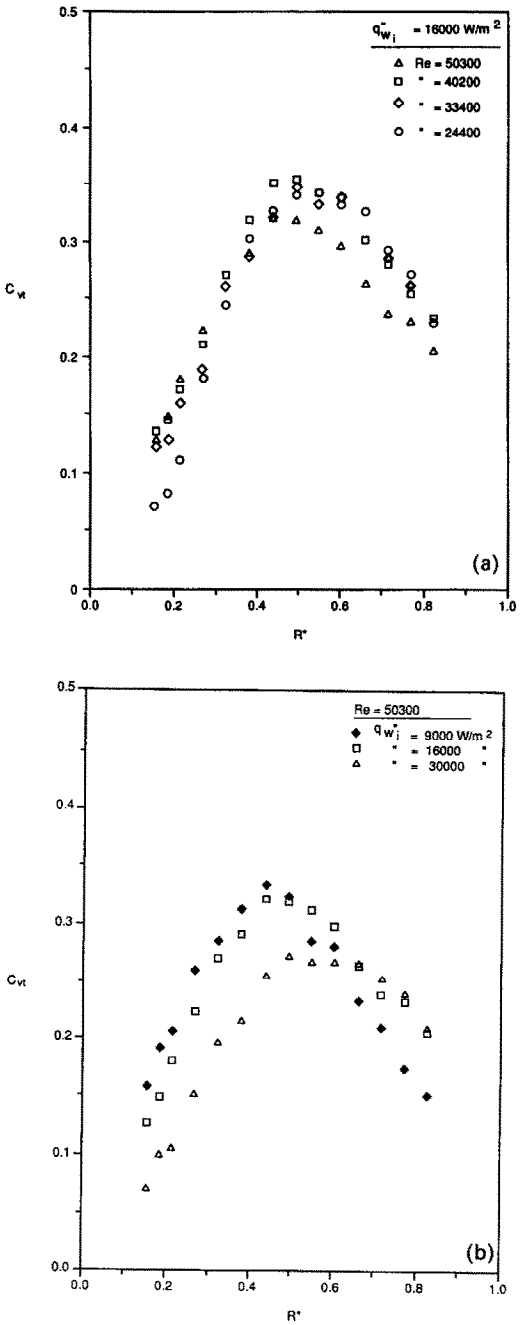

FIG. 14. (a) Radial velocity–temperature correlation coefficient profiles at a wall heat flux of 16000 W m^{-2} and various Reynolds numbers. (b) Radial velocity–temperature correlation coefficient profiles at a Reynolds number of 50300 and various wall heat fluxes.

† The small annulus gap dimension ($\approx$11 mm) was predicated on the requirements of flow boiling experiments performed in the same test section.

thereby adversely affecting the velocity field measurements. This does not appear to have been a problem since the velocity field measurements (mean, intensity, shear stress) remained essentially unchanged when the phase-lead compensation circuit was removed from the temperature sensor signal path. The implication is that adequate temperature compensation was provided by the mean and low frequency portion (i.e. the coarser spatial scales portion) of the temperature signal.

In retrospect, however, a probe design in which the temperature sensor was closer to the x-sensors (e.g. within 0.5 mm) would have been superior in carrying out velocity–temperature correlation measurements.

CONCLUDING REMARKS

Simultaneous velocity and temperature field measurements were carried out in turbulent liquid flow at heated conditions in this effort. A miniature three-sensor anemometer probe was used. The velocity field (including Reynolds normal and shear stresses) data obtained are believed to be significantly more accurate and cover a wider range of flow conditions than the data reported in our earlier work [4]. Both dimensional and nondimensional data are presented with the hope that they will be useful in turbulence modeling efforts.

We were less successful in the measurement of the interdependence between the turbulent velocity and temperature fields. This is apparent from the radial velocity–temperature correlation distributions presented. The main cause of this difficulty appears to have been the relatively large spacings between the sensors of the anemometer probe compared to the flow channel dimension. It may, however, be difficult to reduce the sensor spacings by any significant amount because of probe manufacturing considerations.

One of the authors (RPR) is, at present, embarking on an experimental program in which a laser Doppler velocimeter will be used in conjunction with a fast microthermocouple ($\tau \approx 3$ ms) to carry out turbulent velocity and temperature field measurements with, it is hoped, better results.

Acknowledgement—This work was supported by Electric Power Research Institute, Nuclear Power Division, under research project RP2614.

REFERENCES

1. B. S. Petukhov and L. I. Roizen, Generalized relationships for heat transfer in a turbulent flow of gas in tubes of annular section, *High Temp.* **2,** 65–68 (1964).
2. M. R. F. Heikal, P. J. Walklate and A. P. Hatton, The effect of free stream turbulence level on the flow and heat transfer in the entrance region of an annulus, *Int. J. Heat Mass Transfer* **20,** 763–771 (1976).
3. H. Müller-Steinhagen, N. Epstein and A. P. Watkinson, Subcooled boiling and convective heat transfer for heptane flowing inside an annulus and past a coiled wire: Part I—Experimental results, *ASME J. Heat Transfer* **108,** 922–927; Part II—Correlation of data, **108,** 928–933 (1986).
4. R. P. Roy, V. S. Krishnan and A. Raman, Measurements in turbulent liquid flow through a vertical concentric annular channel, *ASME J. Heat Transfer* **108,** 216–218 (1986).
5. A. Hasan, R. P. Roy and S. P. Kalra, Heat transfer measurements in turbulent liquid flow through a vertical annular channel, *ASME J. Heat Transfer* **112,** 247–250 (1990).
6. J. A. Brighton and J. B. Jones, Fully developed turbulent flow in annuli, *J. Basic Engng* **86,** 835–844 (1964).
7. C. J. Lawn and C. J. Elliott, Fully developed turbulent flow through concentric annuli, *J. Mech. Engng Sci.* **14,** 195–204 (1972).
8. K. Rehme, Turbulence measurements in smooth concentric annuli with small radius ratios, *J. Fluid Mech.* **72,** 189–206 (1975).
9. R. J. Wilson, Correlation and spectral measurement of fluctuating pressure and velocities in annular turbulent flow, Ph.D. Dissertation, University of Illinois, Urbana-Champaign (1979).
10. A. Hasan, Turbulent subcooled boiling and nonboiling flow through a vertical concentric annular channel, Ph.D. Dissertation, Arizona State University, Tempe (1991).
11. R. P. Roy, P. Jain and S. P. Kalra, Dynamic instability experiments in a boiling flow system, *Int. J. Heat Mass Transfer* **31,** 1947–1952 (1988).
12. R. Chevray and N. K. Tutu, Simultaneous measurements of temperature and velocity in heated flows, *Rev. Scient. Instrum.* **43,** 1417–1421 (1972).
13. M. Hishida and Y. Nagano, Simultaneous measurements of velocity and temperature in nonisothermal flows, *ASME J. Heat Transfer* **100,** 340–345 (1978).
14. S. J. Kline and F. A. McClintock, The description of uncertainties in single-sample experiments, *Mech. Engng* **75,** 3–9 (1953).
15. W. E. Burchill, Statistical properties of velocity and temperature in isothermal and nonisothermal turbulent pipe flow, Ph.D. Dissertation, University of Illinois, Urbana-Champaign (1970).
16. M. Hishida, Y. Nagano and M. Tagawa, Transport processes of heat and momentum in the wall region of turbulent pipe flow, *Proc. Eighth Int. Heat Transfer Conf.*, Vol. 3, pp. 925–930 (1986).
17. K. Bremhorst and K. J. Bullock, Spectral measurement of turbulent heat and momentum transfer in fully developed pipe flow, *Int. J. Heat Mass Transfer* **16,** 2141–2154 (1973).
18. C. S. Subramanian and R. A. Antonia, Effect of Reynolds number on a slightly heated turbulent boundary layer, *Int. J. Heat Mass Transfer* **24,** 1833–1846 (1981).
19. H. Tennekes and J. L. Lumley, *A First Course in Turbulence*. The MIT Press, Cambridge, Massachusetts (1972).

CHAMPS DE TEMPERATURE ET DE VITESSE DANS UN ECOULEMENT LIQUIDE TURBULENT

Résumé—Les champs de température et de vitesse sont mesurés dans un écoulement ascendant turbulent de R-113 à travers un espace annulaire vertical concentrique. On rapporte les données expérimentales pour un nombre de Reynolds variant entre 18 000 et 50 300 et un flux thermique pariétal entre zéro et 30 000 W m^{-2}. Les mesures du champ de vitesse sont satisfaisantes bien que des difficultés soient rencontrées pour la mesure des corrélations en un même point entre les fluctuations turbulentes vitesse–température.

GESCHWINDIGKEITS- UND TEMPERATURFELDER IN TURBULENTER FLÜSSIGKEITSSTRÖMUNG

Zusammenfassung—Die Geschwindigkeits- und Temperaturfelder bei turbulenter Aufwärtsströmung von flüssigem R113 in einem senkrechten konzentrischen Ringspalt werden gemessen. Die Bereiche der Reynolds-Zahl und der Wärmestromdichte an der Innenwand betragen 18 000–50 300 bzw. 0–30 000 W m^{-2}. Die Geschwindigkeitsmessungen waren im allgemeinen erfolgreich, während es zu einigen Schwierigkeiten bei der Messung von Einzelpunktkorrelationen zwischen dem turbulenten Schwanken von Geschwindigkeit und Temperatur kam.

ПОЛЯ СКОРОСТЕЙ И ТЕМПЕРАТУР ПРИ ТУРБУЛЕНТНОМ ТЕЧЕНИИ ЖИДКОСТИ

Аннотация—Экспериментально определялись поля скоростей и температур при турбулентном восходящем течении жидкого фресна 113 по вертикальному концентрическому кольцевому каналу. Представлены данные для интервала изменения числа Рейнольдса 18 000–50 300 и диапазона изменения плотности теплового потока на внутренней стенке 0–30 000 Вт. $м^{-2}$. Удалось измерить поле скоростей, в то время как определение одноточечных корреляций между флуктуациями турбулентной скорости и температуры было сопряжено с некоторыми трудностями.